

Surface chemistry models for GaAs epitaxial growth and hydride cracking using reacting flow simulations

Malik Hassanaly,^{1, a)} Hariswaran Sitaraman,¹ Kevin L. Schulte,² Aaron J. Ptak,² John Simon,² Kevin Udway,³ Jacob H. Leach,³ and Heather Splawn³

¹⁾Computational Science Center, National Renewable Energy Laboratory

²⁾Chemistry & Nanoscience Department, National Renewable Energy Laboratory

³⁾Kyma Technologies, Inc.

(Dated: 27 September 2021)

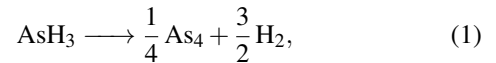
Hydride Vapor Phase Epitaxy (HVPE) is a promising technology that can aid in the cost reduction of III-V materials and devices manufacturing, particularly high-efficiency solar cells for space and terrestrial applications. However, recent demonstrations of ultra fast growth rates ($\sim 500 \mu\text{m/h}$) via uncracked hydrides are not well described by present models for the growth. Therefore, it is necessary to understand the kinetics of the growth process and its coupling with transport phenomena, so as to enable fast and uniform epitaxial growth. In this work, we derive a kinetic model using experimental data and integrate it into a computational fluid dynamics simulation of an HVPE growth reactor. We also modify an existing hydride cracking model that we validate against numerical simulations and experimental data. We show that the developed growth model and the improved cracking model are able to reproduce experimental growth measurements of GaAs in an existing HVPE system.

PACS numbers: 72.80.Ey, 68.43.Mn, 47.11.-j, 81.15.Gh

I. INTRODUCTION

The following article has been accepted by Journal of Applied Physics. After it is published, it will be found at [Journal of Applied Physics](#).

III-V solar cells have been used for decades in space-based applications^{1,2} due to their high specific power and radiation resistance. There is an increasing push to lower the cost of these light, flexible, high-efficiency devices so that they can be used in terrestrial applications, including in transportation, building integration, and consumer electronics. Entry into these markets requires driving down the cost of III-V material manufacturing, and the recent re-emergence of hydride vapor phase epitaxy (HVPE) is one possible pathway to do so³. HVPE uses relatively low-cost precursors, uses them efficiently, and recently showed growth rates for GaAs and GaInP over 500 and 200 $\mu\text{m/h}$ ^{4,5} respectively, which could have a significant effect on overall costs⁶. It is the use of uncracked hydride precursors, in this case, AsH₃ and PH₃, that enables these high growth rates using HVPE⁷. The active hydrogen released from the hydride molecule at the growth surface is theorized to scavenge chemisorbed Cl atoms that otherwise act to inhibit growth⁸. This hydride-enhanced mechanism significantly reduces the kinetic barrier to growth, allowing for rates exceeding 500 monolayers/s at moderate growth temperatures ($\sim 900 \text{ K}$) that are conducive to the formation of other alloys, e.g. GaInP, needed for standard solar cell device structures. Previous work by DenBaars *et al.*⁹ showed that AsH₃ could spontaneously crack at quartz surfaces following the global surface reaction



which they modeled with a one-step chemical mechanism. A method to inhibit arsine cracking at the substrate is to increase the velocity of the carrier gas, thereby limiting the residence time of arsine in the hot portion of the reactor. However, larger velocities can adversely affect external gas sources mixing and lead to a non-uniform growth at the substrate, requiring careful design of the growth system. Furthermore, since surface growth is faster, the coupling with gas transport is stronger in hydride-enhanced HVPE growth. In this context, a simulation-based understanding that couples the chemical kinetics of arsine cracking and GaAs deposition with transport phenomena is paramount for the optimization of the overall manufacturing process.

Existing growth models for the deposition of GaAs in the literature only consider deposition from arsenic vapor (As₂ or As₄)^{10,11}, but not from uncracked AsH₃. In this work, a one-step kinetic model for the deposition of GaAs from uncracked arsine and gallium chloride is developed and describes the following global reaction



The main contributions of the paper are: a) the development of a kinetic model for surface growth of uncracked arsine; b) uncertainty bounds on the growth model parameters are provided using a Bayesian calibration approach; c) an update of the arsine cracking model of DenBaars *et al.*⁹; d) the cracking and growth models are integrated into a computational fluid dynamics (CFD) solver.

The surface growth model is developed and validated by modeling the reaction kinetics and the fluid dynamics in a lab-scale reactor designed for a 2-inch substrate, and for which

^{a)}Electronic mail: malik[dot]hassanaly[at]nrel[dot]gov

experimental growth data is available. The rest of the paper is organized as follows. Section II presents the lab-scale reactor simulated and the dataset used to develop the kinetic model. The numerical method is described in Sec. III and the calibration of the cracking model from experimental data is shown in Sec. IV. In Sec. V, the finite rate kinetic model for GaAs deposition is developed. Concluding remarks are provided in Sec. VI.

II. CONFIGURATION AND EXPERIMENTAL DATASET

A. D-HVPE reactor

The configuration simulated in this work (see illustration in Fig. 1) is from experimental studies by Schulte *et al.*⁷ that used a Dynamic-Hydride Vapor phase epitaxy (D-HVPE) reactor where growth rates with uncracked arsine were also reported. These experiments were conducted with a Dynamic-Hydride Vapor phase epitaxy (D-HVPE) reactor¹² which addresses manufacturing challenges posed by HVPE. Highly efficient thin-film solar cells typically consist of several layers, each one made of a different III-V compound¹³. When the growth rate of the solar cell is low enough and the reactor equilibrates quickly, the substrate can be kept idle in the same chamber while different external gas are injected over time. With a higher growth rate and large residence time of gases - such as in HVPE deposition reactors - this strategy can lead to non-abrupt interfaces between the layers, which is detrimental to solar cell efficiency. In the D-HVPE, the aforementioned issue is avoided by physically moving the substrate to a different chamber each time a new layer needs to be grown. In order to prevent inter-chamber flow contamination, the chambers are separated by vertical gas curtains created by a flow of H₂ (see illustration in Fig. 1).

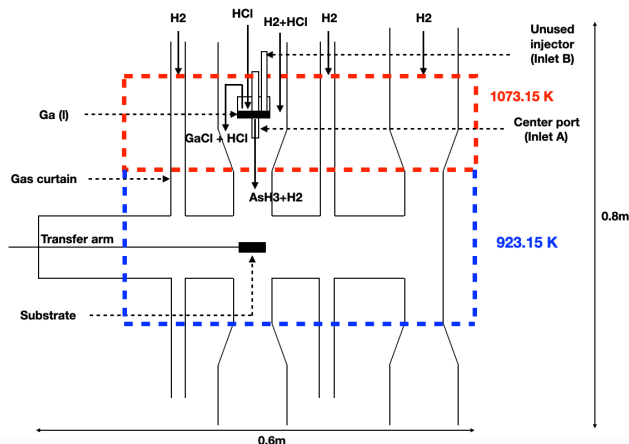


FIG. 1. Schematic of the D-HVPE reactor. Solid arrows indicate flows, while dashed arrows point to different elements of the reactor. An external furnace maintains part of the reactor wall temperature at 1073.15 K (area surrounded by --) and the rest at 923.15 K (area surrounded by - -).

The D-HVPE reactor considered here has been

experimentally^{5,7,14} and numerically^{4,14} shown to provide high growth rate and efficiency, while potentially enabling in-line manufacturing.

The metal-halide is generated in-situ by injecting HCl into a boat/reservoir of liquid Ga. The boat is externally heated at 1073.15 K to drive the kinetics of the $\text{HCl} + \text{Ga} \rightarrow \text{GaCl}$ reaction. The boat conversion efficiency was previously estimated to be 90%¹⁵. It outputs a mixture of gaseous gallium chloride GaCl and residual HCl that were not converted. A center port (called inlet A in Schulte *et al.*⁷) introduces a mixture of AsH₃ and H₂ in the chamber. The reactants are then deposited on a substrate externally heated at 923.15 K. In Fig. 1, the external heating is represented by the red and blue dashed boxes.

B. Dataset

The dataset used for validation of our model is that presented in Schulte *et al.*⁷ where growth rates at the center of the substrate were measured under a variety of flow conditions. The volume flow rates at standard pressure and temperature for all the cases considered are shown in Tab. I. The experiments were conducted at a pressure of 0.829 atm and with external gas injected at ambient temperature.

TABLE I. Volume flow rates in standard centimeter cubes per minute (sccm) for each case simulates. "Top Chamber" denotes the top boundary of the chamber that contains the substrate. "Adjacent Chamber" denotes the top boundary of the chamber that does not contain the substrate.

[sccm]	Center Port		Top Chamber			Adjacent Chamber	Curtains
Case	H ₂	AsH ₃	H ₂	HCl	GaCl	H ₂	H ₂
Case 1	1000	44.5	8200	21	9	10000	2500
Case 2	1600	44.5	7600	21	9	10000	2500
Case 3	2200	44.5	7000	21	9	10000	2500
Case 4	2500	33.5	7500	20.8	7.2	10000	2500
Case 5	2500	33.5	7500	21	9	10000	2500
Case 6	2500	33.5	7500	21.2	10.8	10000	2500
Case 7	2500	33.5	7500	21.6	14.4	10000	2500

An important observation from the experiment was the near-zero growth of GaAs when AsH₃ was recirculated into the reactor (through inlet B in Fig. 1) similar to GaCl rather than direct injection through the center port (inlet A in Fig. 1). The larger residence time of AsH₃ in this case led to increased cracking at the reactor walls before reaching the substrate. This hypothesis is further bolstered by the success of growth rate models that considered a deposition pathway only via cracked arsine¹⁴. Under the conditions where all the arsine has cracked and in the range of operating conditions investigated, an equilibrium kinetic model¹⁵ indeed predicts growth rates of at most 2 $\mu\text{m/h}$ (Fig. 2) which is at least one order of magnitude lower than growth rates measured in Schulte *et al.*⁷. Here, the As₄ pathway is inhibited by the low residence time of external gas sources and the low substrate temperature. Therefore, the growth rate available in Schulte *et al.*⁷ is particularly suited to deduce a kinetic model for the

AsH₃-pathway for epitaxial growth.

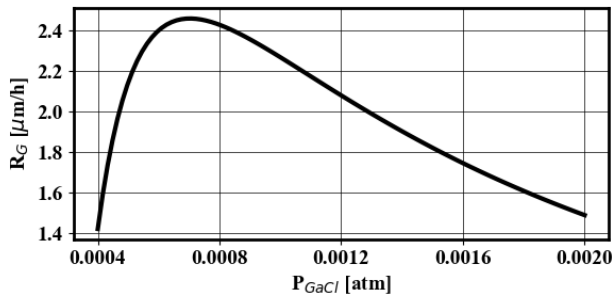


FIG. 2. GaAs(s) growth rate via As₄ reaction pathway at 923.15 K for various partial pressure of GaCl.

III. NUMERICAL METHOD

To derive a kinetic model for the surface reaction via uncracked hydrides, computational fluid dynamics (CFD) simulations of the experimental configuration are conducted. The kinetic model depends on parameters that are then calibrated to match experimental growth rates. The fluid solver used is described in App. A, the implementation of surface reactions is explained in App. B and the transport and thermodynamic parameters are given in App. C.

The boat injector is omitted from the domain to simplify the geometry. Instead, the boat injector is modeled using an injector spread over the top of the chamber aligned with the substrate, assuming uniform composition of GaCl, HCl and H₂. The volume flow rates for the top chamber are available in Tab. I. Additionally, to reduce the range of scales resolved, the inner region of the center port is not meshed and its exit is treated as an inlet boundary condition. Because AsH₃ is mostly exposed to walls inside the center port, this is where it mostly cracks. The boundary conditions at the exit of the center port need specific treatment to incorporate this effect and are described in App. D.

A hexahedral-dominant mesh shown in Fig. 3 is used with refinement near the injector exit and the platter, where large gradients of velocity and composition are observed. To ensure that the results presented are not influenced by numerical errors, two different meshes are used by increasing the resolution in the chamber that contains the substrate. The coarse mesh contains about 0.5 million computational cells and the finer mesh consists of 1 million cells. The smallest mesh size in all three directions is 0.75 mm and 0.47 mm for the coarse and fine meshes, respectively.

IV. ARSINE CRACKING MODEL

As mentioned in Sec. I, the cracking of hydrides (here AsH₃) critically impacts the growth rate of GaAs layers. Therefore, a cracking kinetic model needs to be included with

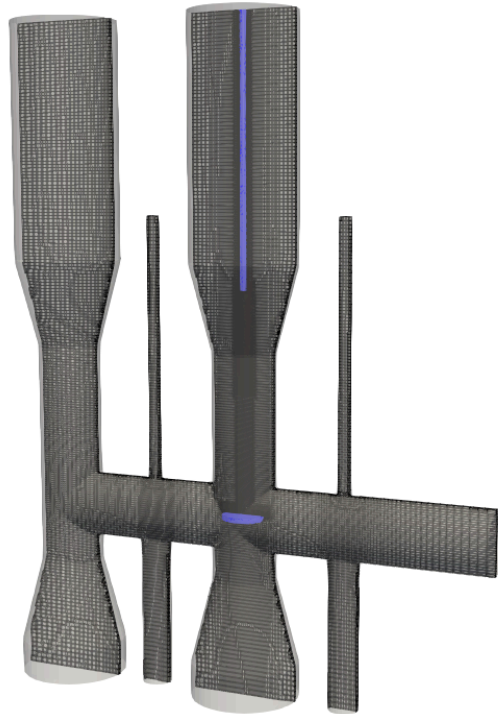


FIG. 3. Illustration of the mesh used. The blue parts denote the center port and the substrate. Note the refinement near the center port exit and near substrate, where gradients are the largest.

other surface reactions and coupled with the transport equations to adequately predict deposition rates. A global kinetic model for the decomposition of hydrides at quartz surfaces (the walls of the D-HVPE reactor considered here are also made of quartz) of AsH₃ diluted within a H₂ carrier gas was developed in DenBaars *et al.*⁹. One of the experiments reported in DenBaars *et al.*⁹ included measurement of AsH₃ concentration after it has passed through a 5 cm diameter and 12.5 cm long heated quartz tube at a speed of 1.25 cm/s. The kinetic rate of the global reaction (Eq. 1) was modeled in the Arrhenius form as

$$K_{cracking} = A_{cracking} \exp\left(-\frac{E_{a_{cracking}}}{R_u T}\right), \quad (3)$$

where $A_{cracking}$ and $E_{a_{cracking}}$ are constant kinetic coefficients for pre-exponential factor and activation energy, R_u is the universal gas constant, and T is the surface temperature. The values reported for $K_{cracking}$ by DenBaars *et al.*⁹ were computed by assuming with respect to volumetric arsine concentration, given by

$$K_{cracking} = \frac{1}{\Delta t} \log\left(\frac{C_0}{C_f}\right), \quad (4)$$

where Δt is the residence time of the gas in the quartz tube, C_0 and C_f are the volumetric molar concentrations of AsH_3 at the inlet and outlet of a tube through which a mixture of arsine and hydrogen flowed. While the expression of Δt is not explicitly given, the value of $K_{cracking}$ provided in DenBaars *et al.*⁹ suggests that it was calculated as $\frac{L}{U}$, where L is the length of the tube and U is the streamwise velocity. The expression chosen for $K_{cracking}$ neglected the effect of surface-to-volume ratio which depends on the geometry of the tube. For instance, if the tube had a smaller diameter, and under the same conditions as the experiments – in particular same volume flow rates –, the apparent $K_{cracking}$ would be larger than the one seen in the experiments. The importance of including geometry considerations in the kinetic constants was also recognized elsewhere¹⁶. Furthermore, since $K_{cracking}$ is the rate constant for a surface reaction it should have units of $\text{m}\cdot\text{s}^{-1}$. DenBaars *et al.*⁹ factored in the area-to-volume ratio (units of m^{-1}) within $K_{cracking}$ that gave rise to a first-order rate constant with units of $1/\text{s}$. The authors reported a value for $E_{a_{cracking}} = 34 \text{ kcal/mol}$ by varying the temperature of the tube but did not propose a value for $A_{cracking}$. One of the main contributions of this work is the calibration of $A_{cracking}$ along with a correction to the expression for $K_{cracking}$ that accounts for the surface-to-volume ratio.

One can estimate the cracking of AsH_3 in a cylindrical tube using a steady one dimensional advection-reaction equation (justification is provided in App. D). The mass fraction of arsine Y_{AsH_3} along the streamwise direction follows the relation

$$\pi R^2 \frac{d}{dx} (\rho U Y_{\text{AsH}_3}) = -K_{cracking} \rho Y_{\text{AsH}_3} 2\pi R, \quad (5)$$

where U is the streamwise velocity and R is the tube radius. Assuming that the density ρ varies only due to temperature variations, one can derive an approximate relation for the ratio C_f/C_0 as

$$K_{cracking} = \frac{UR}{2L} \log \left(\frac{C_0}{C_f} \right). \quad (6)$$

The new pre-log factor can be thought of as a residence timescale rescaled with a non-dimensional ratio of catalytic surface per unit volume. With that rescaling, the cracking kinetic coefficient now includes the effect of tube radius and the expression can be directly used to obtain a value for $A_{cracking}$ by fitting the experimental data to the 1D model.

To incorporate modeling and experimental uncertainty in the calibration of $A_{cracking}$, a Bayesian calibration approach is adopted^{17,18}. The output of that procedure is a posterior probability density function (PDF) of $A_{cracking}$ given the experimental data available and is computed as

$$P(A_{cracking}|D) \sim P(D|A_{cracking})P(A_{cracking}), \quad (7)$$

where $P(A_{cracking}|D)$ is the posterior PDF, $P(A_{cracking})$ is a prior PDF (describes the knowledge of $A_{cracking}$ without

any experimental measurement) and $P(D|A_{cracking})$ is the likelihood of the data. An uninformative prior $P(A_{cracking}) \sim \mathcal{U}(10^4, 2 \times 10^7)$ is chosen. Following Braman, Oliver, and Raman¹⁷, a Gaussian likelihood is adopted,

$$P(D|A_{cracking}) \sim \frac{1}{(2\pi\sigma)^{N_d/2}} \exp \left[-\frac{1}{2\sigma^2} \sum_{i=1}^{N_d} (x_i(A_{cracking}) - D_i)^2 \right], \quad (8)$$

where N_d is the number of data points, x_i is the model prediction for the i^{th} experiment, D_i is the i^{th} experimental value, and σ is a hyperparameter which describes the experimental errors. Since σ is unknown here, it is fit as part of the Bayesian calibration procedure with prior $\mathcal{U}(0, 10)$, along with $A_{cracking}$ ¹⁷. It was found that the choice of prior had little influence on the calibrated parameters (shown in App. E. The results of the Bayesian calibration are shown in Fig. 4.

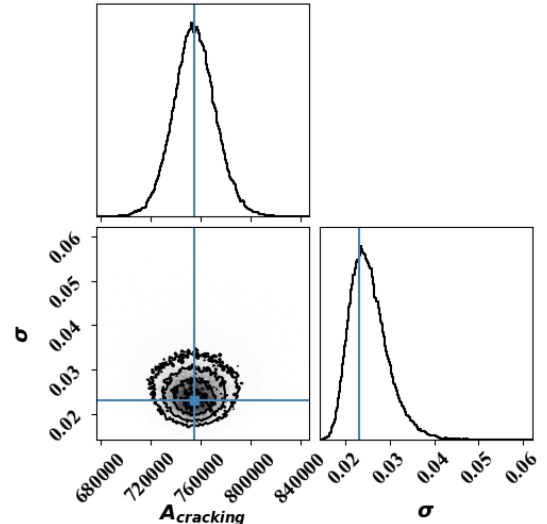
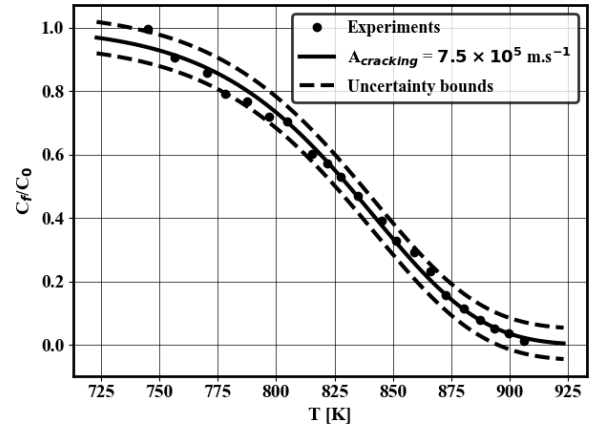


FIG. 4. Top: experimental measurement (●) of AsH_3 cracking at different temperatures, 1-step cracking model prediction with $A_{cracking} = 7.5 \times 10^5 \text{ m}\cdot\text{s}^{-1}$ (—) corresponding to the largest posterior probability and uncertainty bounds $\pm\sigma$ (- -). Bottom: corner plot of the 2-dimensional posterior PDF.

V. GALLIUM ARSENIDE GROWTH MODEL

A. Model functional form

The surface reaction is modeled as an irreversible forward reaction



The assumption of irreversibility is justified by its large equilibrium constant which suggests that the backward reaction is unlikely^{4,19}. A finite rate chemistry model is developed hereafter for the forward reaction. An infinitely fast model is also constructed and the results are reported in App. F.

The finite rate chemistry model for the reaction at the substrate is constructed by assuming the Arrhenius form $K_{\text{reac}} = A_{\text{reac}} T^{\beta_{\text{reac}}} \exp(-Ea_{\text{reac}}/R_u T)$, where A_{reac} , β_{reac} are kinetic constants and Ea_{reac} is the activation energy. In the experiments conducted in Schulte *et al.*⁷, it was found that for the temperature range [873 – 953 K], the dependence of the epitaxial growth rate with temperature was negligible. Therefore, K_{reac} is assumed to be independent of temperature over similar temperature ranges studied in this work.

The objective of this section is to find a value of K_{reac} . The CFD model is used to simulate the D-HVPE reactor with different values of K_{reac} . The resulting growth rates are obtained by computing the molar flux of AsH_3 at the substrate, which is equal to the number of moles of GaAs produced. The density of GaAs(s) is then used to compute the growth rate obtained via CFD, which is then compared to the ones reported in the Schulte *et al.*⁷. The growth rates are measured at the center of the substrate.

B. Model calibration

Eleven values of K_{reac} are chosen within the range [45 m.s⁻¹, 310 m.s⁻¹]. For each value of K_{reac} , the seven cases shown in Tab. I are simulated. In absence of uncertainty, a total of 77 numerical simulations would be needed for calibration. In the present case, the optimal value of K_{reac} depends on the value of A_{cracking} obtained by fitting the cracking model. To account for uncertainty in the value of A_{cracking} , the calibration procedure is conducted for ten values of A_{cracking} chosen in the range [6.5 × 10⁵ m.s⁻¹, 8.5 × 10⁵ m.s⁻¹], which span the support of its posterior distribution. The function that related K_{reac} and A_{cracking} is then convolved with the posterior distribution of A_{cracking} to deduce the PDF of K_{reac} . The overall procedure is illustrated in Fig. 5 and requires a total of 770 runs.

Due to the large number of simulations required, the calibration is done with the coarse grid (0.5 million computational cells). The fine mesh (1 million computational cells) is used afterwards to verify grid convergence for the estimated values of K_{reac} .

C. Results

The steady-state distribution of temperature and arsine mass fraction for case 3 (Tab. I) with $K_{\text{reac}} = 222.8 \text{ m.s}^{-1}$ and $A_{\text{cracking}} = 8.5 \times 10^5 \text{ m.s}^{-1}$ is illustrated in Fig. 6. It can be seen that since the flow inside the center port is heated to a temperature close to 1073.15 K, the center port injects a hot flow at the substrate (indicated by the arrow). The contour of AsH_3 (bottom) shows the effect of the flow curtain which avoids contamination of the adjacent chamber with arsine (left arrow). At the substrate, AsH_3 is consumed, which results in a non-zero normal gradient (right arrow). Similar features can be observed for GaCl.

For each ($K_{\text{reac}}, A_{\text{cracking}}$) sample pair, the average error in growth rate $\langle \epsilon \rangle$ over the seven cases considered is computed. The results are shown in Fig. 7. It can be seen that there exists an optimal value of K_{reac} which leads to the best match of the growth rates. In the particular case considered ($A_{\text{cracking}} = 8.5 \times 10^5 \text{ m.s}^{-1}$), $K_{\text{reac}} = 222.8 \text{ m.s}^{-1}$ minimizes $\langle \epsilon \rangle$. To improve the estimate of the value of K_{reac} that minimizes the error, interpolation between data points is done with radial basis functions, where hyperparameters are optimized using the Scikit-Learn library²⁰. An example of the interpolation result is shown in Fig. 7.

Over the range chosen K_{reac} , it can be observed from Fig. 7 that there exists a value that can serve, at least, as a global minimizer of the discrepancy with experimental results. It is shown here, that the local minimum is likely a global minimum. We first argue that the relationship between the rate of growth R_G and the kinetic coefficient K_{reac} is monotonic and increasing. Physically, this assertion is justified by the fact that increasing the kinetic rate should increase the rate of production of GaAs. We also propose a numerical argument by plotting the difference between the rate of growth obtained in the simulations ($R_{G,\text{sim}}$) and in experiments ($R_{G,\text{exp}}$) for all A_{cracking} and all K_{reac} values. The results are shown in Fig. 8 (top). As expected, the rate of growth is monotonically increasing with K_{reac} for all A_{cracking} values. Next, we record the minimum and maximum error over all the cases for each A_{cracking} and K_{reac} . Because of the monotonically increasing relation between K_{reac} and R_G , if the maximum error $R_{G,\text{sim}} - R_{G,\text{exp}}$ at the lowest K_{reac} value is negative, then $\forall K_{\text{reac}} < 45 \text{ m.s}^{-1}$, $\langle \epsilon \rangle$ would be larger than for $K_{\text{reac}} = 45 \text{ m.s}^{-1}$. In Fig. 8 (right), it can be seen that the maximum absolute value of the error is almost negative for all A_{cracking} at $K_{\text{reac}} = 45 \text{ m.s}^{-1}$. The same argument can be invoked for the minimum error at $K_{\text{reac}} = 310 \text{ m.s}^{-1}$ which is positive. We therefore argue that the minimum shown is likely a global minimum.

The growth rates computed with $K_{\text{reac}} = 222.8 \text{ m.s}^{-1}$ and $A_{\text{cracking}} = 8.5 \times 10^5 \text{ m.s}^{-1}$ are plotted against experimental values in Fig. 9. A reasonable agreement with experiments can be observed. Furthermore, the trends are consistent with the experiments and physical intuition. As the volume flow rate of H_2 , Q_a through the center port increases (left), less AsH_3 cracks which leads to larger reaction rates. The exponential dependence of the amount of cracked AsH_3 with the velocity (Eq. D3) should result in a super-linear increase of

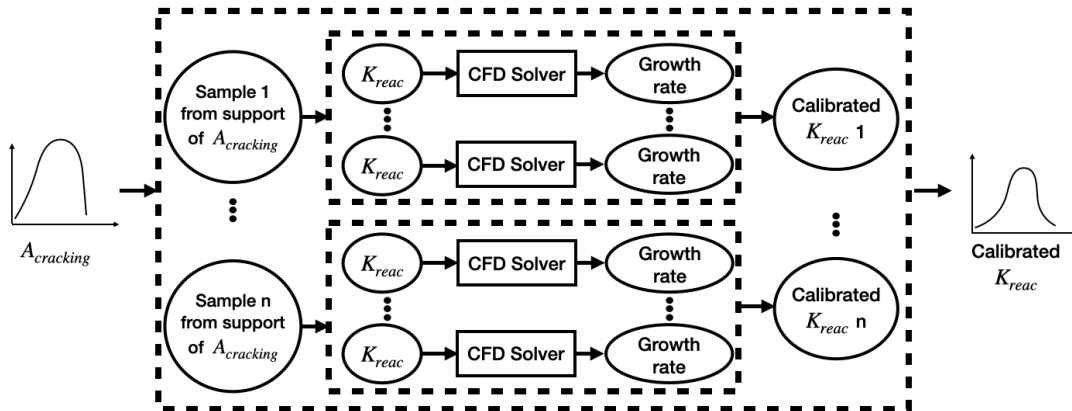


FIG. 5. Illustration of the workflow of the calibration procedure.

growth rate with the flow rate of arsine through the center port. This is the trend observed in the experiments and the simulations. This observation is in sharp contrast with the linear increase of the growth rate with increasing concentration of GaCl (bottom). To ensure that the calibrated K_{reac} is only minimally affected by the numerical errors, the fine grid (1 million computational cells) is used to verify that the results are grid converged. The fine and coarse grids predict similar growth rates and therefore the baseline grid is sufficient for accurate predictions.

The spatial distribution of the growth rate at the substrate is compared to experimental data in Fig. 10. A reasonable agreement can be observed for case 3 (strong flow through the center port). A breakdown of the axial symmetry can be observed for case 2 (weaker flow through the center port) both in simulation and experimental data. The apparent breakdown of symmetry typically appears at low center port velocity, such as the one of Case 2. The flow near the substrate is influenced by a vertical component that originates from the center port, and by a horizontal component, the crossflow that connects the two deposition chambers. The horizontal flow can be observed in Fig. 6 (middle and bottom). When lower center port velocities are used, the relative effect of the horizontal crossflow may increase and disturb the boundary layer near the substrate, thereby leading to a breakdown of growth symmetry. Interestingly, the same symmetry breakdown seems to occur in the experimental results, albeit to a smaller extent. The discrepancy may be due to a slightly earlier center port jet breakdown in the simulations due to either numerical diffusion, or errors in the center jet exit boundary conditions. Finally, we note that in other experiments reported for the same reactor¹⁴, a similar breakdown of symmetry may appear at different conditions. This result suggests that the model can be used not only to assess the overall growth rate of the substrate but also its spatial uniformity, which is critical for the efficiency of solar cells.

As explained in Sec. V B, the calibration procedure is repeated for ten different values of $A_{cracking}$ which span the support of its posterior distribution obtained in Sec. IV. As a re-

sult, one obtains the response curve of the optimal K_{reac} as a function of $A_{cracking}$, which is shown in Fig. 11 (top). As $A_{cracking}$ increases, the amount of AsH_3 that reaches the substrate decreases. Therefore, to keep constant the growth rates, the optimal K_{reac} is a monotonically increasing function of $A_{cracking}$. This trend can be observed in Fig. 11. It can however be seen that the increase occurs by steps which is a consequence of the discretization of $A_{cracking}$. Given the dependence of K_{reac} with $A_{cracking}$, one can sample $A_{cracking}$ using a Markov-chain Monte Carlo (MCMC) approach and construct a PDF of K_{reac} . The results are shown in Fig. 11 (bottom). The standard deviation of the PDF of K_{reac} can then be used to extract uncertainty bounds on the calibrated value of the kinetic parameter. We found $K_{reac} = 205 \pm 5 \text{ m.s}^{-1}$

VI. CONCLUSIONS

In this work, a comprehensive modeling procedure was developed for the simulation of growth rate via uncracked hydrides in a D-HVPE reactor. The AsH_3 cracking model was adjusted for the geometry and a surrogate model for the cracking through the injectors was developed. Multiple simulations for the surface reactions at the substrate were used to calibrate a simple kinetic model for the reaction of uncracked arsine. The proposed model matches experimental growth rate values and spatial distributions for a range of typical HVPE operating conditions.

As part of the calibration, an uncertainty quantification procedure was conducted to include uncertainty in the AsH_3 cracking model parameters. While the influence of other uncertain parameters like numerical CFD errors was shown to be negligible, uncertainty due to the interpolation during the calibration procedure will be included as future work.

Since III-V solar cells typically require the growth of different layers, the same procedure will be applied to develop kinetic models that correspond to each one of the compounds. Finally, the validated kinetic model will be used in conjunction with a CFD software to design scaled-up reactors

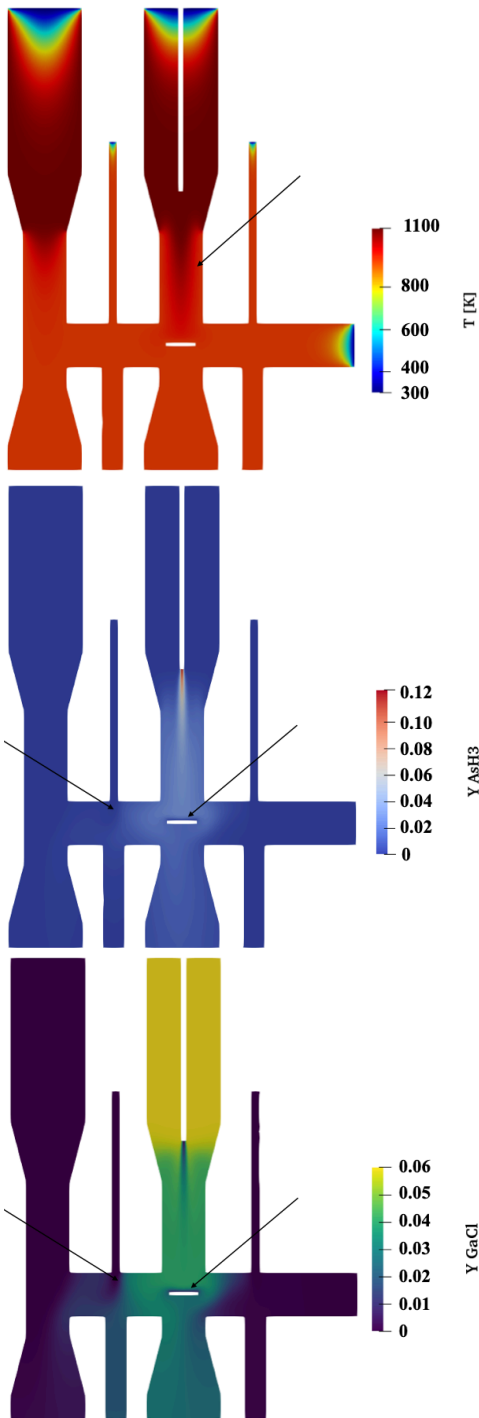


FIG. 6. Top: steady-state contour of temperature in the D-HVPE reactor for Case 3. Middle: steady-state contour of mass fraction of AsH_3 in the D-HVPE reactor for Case 3. Bottom: steady-state contour of mass fraction of GaCl in the D-HVPE reactor for Case 3. Arrows point to regions of interest.

able to maximize growth rate while minimizing growth non-uniformity.

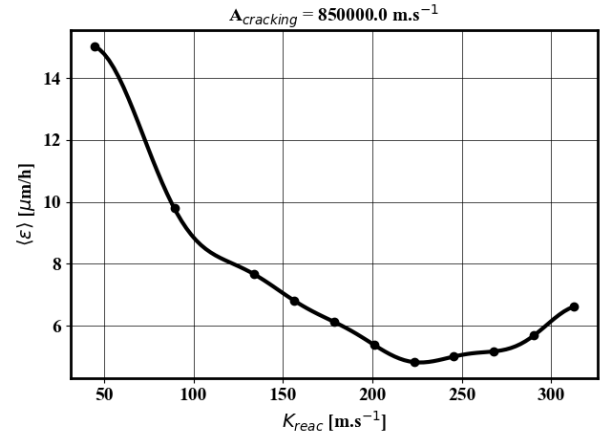


FIG. 7. Average growth rate prediction error across the seven cases investigated as a function of the kinetic constant K_{reac} with $A_{\text{cracking}} = 8.5 \times 10^5 \text{ m.s}^{-1}$. Simulation results (●) and interpolated results with radial basis functions (—) are displayed.

ACKNOWLEDGMENTS

Fruitful discussions with Milo Parra-Alvarez and Olga Doronina are gratefully acknowledged. This work was authored by the National Renewable Energy Laboratory, operated by Alliance for Sustainable Energy, LLC, for the U.S. Department of Energy (DOE) under Contract No. DE-AC36-08GO28308. This work was supported by the Air Force Research Laboratory (IAG-19-02103). This research was performed using computational resources sponsored by the U.S. Department of Energy's Office of Energy Efficiency and Renewable Energy and located at the National Renewable Energy Laboratory. The views expressed in the article do not necessarily represent the views of the DOE or the U.S. Government. The U.S. Government retains and the publisher, by accepting the article for publication, acknowledges that the U.S. Government retains a nonexclusive, paid-up, irrevocable, worldwide license to publish or reproduce the published form of this work or allow others to do so, for U.S. Government purposes.

DATA AVAILABILITY

The data that support the findings of this study are available from the corresponding author upon reasonable request.

Appendix A: Fluid solver

A variable density low-Mach number solver based on the OpenFOAM framework is used²¹ to model the flow inside the reactor. The solver has been successfully applied in several other studies^{22,23} including configuration with reactive phase transformations such as the one considered here²⁴. The low-Mach number assumption allows for the use larger time-

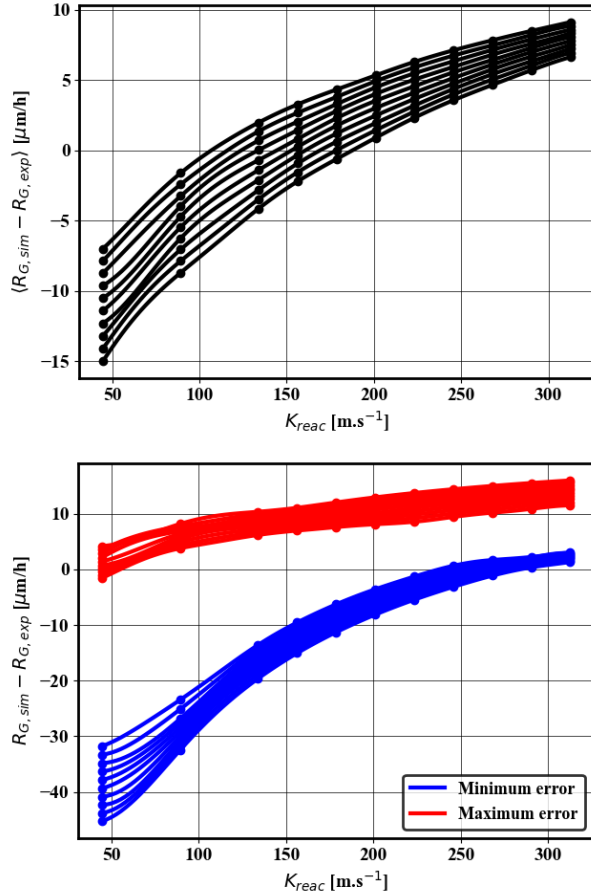


FIG. 8. Left: average difference between the rate of growth obtained from simulations $R_{G,sim}$ and the rate of growth obtained from experiments $R_{G,exp}$ plotted against K_{reac} for all $A_{cracking}$. Right: minimum (—) and maximum (—) difference of the rate of growth obtained from simulations $R_{G,sim}$ compared to rate of growth obtained from experiments $R_{G,exp}$ plotted against K_{reac} for all $A_{cracking}$.

steps on the order of fluid convection time-scales (~ 1 ms) in all the simulations, without the need to resolve acoustic time-scales. Thermodynamics variables (specific heat, enthalpy) and transport properties (viscosity, thermal conductivity, species diffusivity) used in the model are obtained from open source library, *PelePhysics*, designed for complex combustion simulations²⁵.

The momentum transport equation given by:

$$\frac{\partial \rho \mathbf{u}}{\partial t} + \nabla \cdot (\rho \mathbf{u} \mathbf{u}) = -\nabla p + \nabla \cdot \bar{\boldsymbol{\tau}}, \quad (\text{A1})$$

is solved, where the pressure p is computed to ensure mass conservation and $\bar{\boldsymbol{\tau}}$ is the stress tensor.

The gas-phase species are transported using the equation

$$\frac{\partial \rho Y_i}{\partial t} + \nabla \cdot (\rho \mathbf{u} Y_i) = \nabla \cdot (\rho D_i \nabla Y_i) + \dot{\omega}_i, \quad (\text{A2})$$

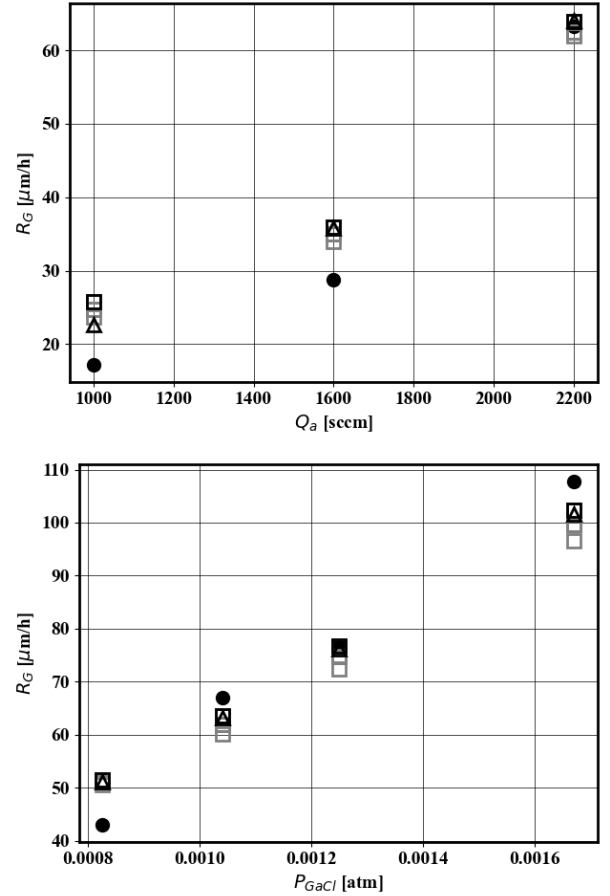


FIG. 9. Growth rate of GaAs comparison between experimental data reported in Schulte *et al.*⁷ (●), the calibrated model used with the 0.5 million cells grid (□) and the calibrated model used with the 1 million cells grid (Δ) for $A_{cracking} = 8.5 \times 10^5 \text{ m.s}^{-1}$. Results are overlaid with calibrated model obtained with the 0.5 million cells grid for all other $A_{cracking}$ values (□). Top: Case 1-3 where growth rate is plotted against Q_a , the volume flow rate of H_2 through the center port. Bottom: Case 4-7 where growth rate is plotted against P_{GaCl} , the partial pressure of GaCl.

where $Y_i \in \{Y_{\text{AsH}_3}, Y_{\text{As}_4}, Y_{\text{GaCl}}, Y_{\text{HCl}}\}$ are species mass fractions, ρ is the gas mixture density, \mathbf{u} is the flow velocity and D_i are the individual species diffusivities. The mass fraction of the carrier specie Y_{H_2} is obtained by enforcing the unity mass fraction sum constraint.

The energy equation is solved in terms of a global temperature among all species given by:

$$\frac{\partial \rho T}{\partial t} + \nabla \cdot (\rho \mathbf{u} T) = \nabla \cdot (\lambda \nabla T) - \rho (\nabla T) \cdot \sum_{i=1}^N C_{p_i} Y_i \mathbf{V}_i + \omega_{HR}, \quad (\text{A3})$$

where T denotes temperature, λ is the thermal conductivity, C_{p_i} are the species heat capacities, \mathbf{V}_i are the species diffusion velocities, N is the number of species, and ω_{HR} denotes the heat release rate.

A Smagorinsky²⁶ turbulence model is used and is mostly

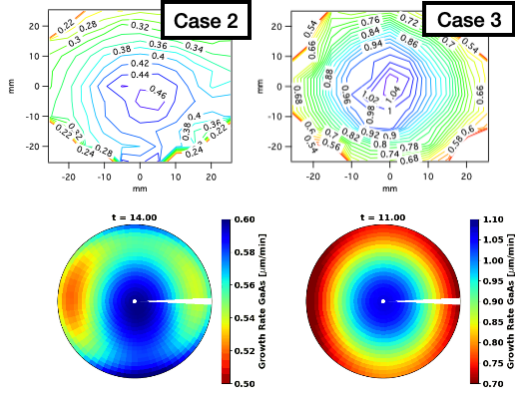


FIG. 10. Spatial distribution of growth rate at the substrate for case 2 (left) and case 3 (right) between experimental data (top) and simulation data (bottom) with $A_{cracking} = 8.5 \times 10^5 \text{ m.s}^{-1}$ and $K_{react} = 222.8 \text{ m.s}^{-1}$.

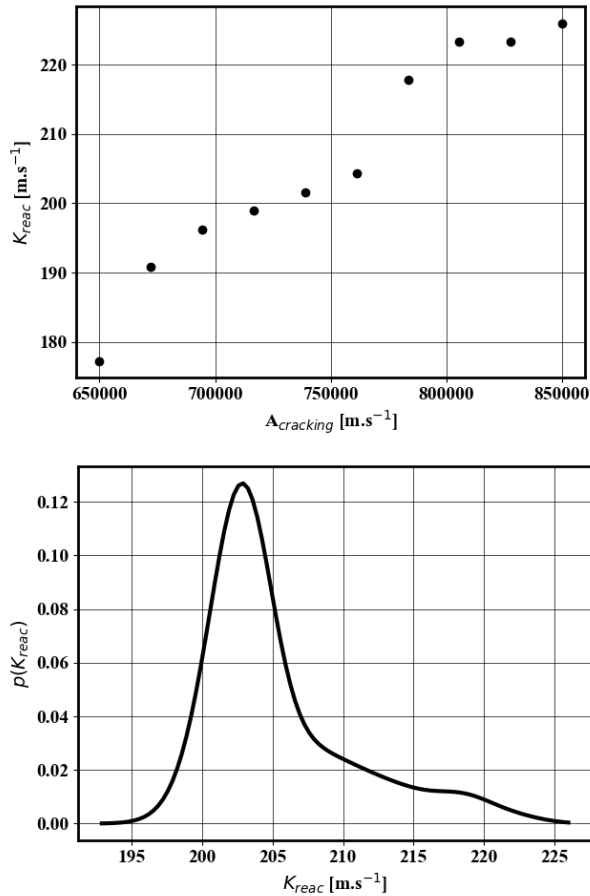


FIG. 11. Top: calibrated value of K_{react} for each value of $A_{cracking}$ considered. Bottom: constructed PDF of K_{react} .

active in the shear layer near the center-port exit, while the flow near the substrate is nearly laminar. For the scalar turbulence, a turbulent Schmidt number $Sc_t = 0.72$ and a turbulent

Prandtl number $Pr = 0.7$ were used²⁷. The turbulence model is useful for stabilization purposes in the shear layers and all the results in this work are obtained when the reactor reaches steady-state.

Appendix B: Numerical implementation of finite-rate surface reactions

The surface reactions are implemented in a fashion similar to Maestri and Cuoci²⁸ by imposing a non-zero flux of species at the walls. Formally, the reaction source term for species i is written as

$$\dot{\omega}_i = \nabla \cdot \Omega_i, \quad (\text{B1})$$

where Ω_i is a field defined at the cell faces which is null everywhere in the domain, except at the walls where surface reactions occur. Ω_i is computed using the kinetic model and by assuming the surface concentration of the species equals that of the volumetric concentration at the computational cell immediately adjacent to the face. The same procedure is used to define the heat release from the walls. The surface reactions are coupled with the scalar transport equation using a Strang splitting method²⁹, except when infinitely fast chemistry is used (See App. F).

The surface reactions in this work involve a conversion of species in the gas phase to solid phase products at the catalytic surfaces. Therefore, mass may leave or enter the gas phase at these surfaces. Similar to other cases where a phase change occurs like with spray evaporation³⁰ or soot formation³¹, the pressure equation needs to be augmented with a source term for mass. The mass source term \dot{m} is simply computed as

$$\dot{m} = \sum_{i=1}^N \dot{\omega}_i, \quad (\text{B2})$$

where N is the number of species.

Appendix C: Thermodynamic and transport parameters

The thermodynamic parameters (enthalpy and calorific capacity) are obtained from polynomial fits that relate them to the local temperature. The coefficients of the polynomial fits are obtained from Oehlschlaeger *et al.*³². Missing properties of GaCl were substituted with the properties of GaH. Note that although the polynomial coefficient for the calorific capacity and enthalpy were substituted, the molar weight (used to compute density) was not modified. Similarly, the transport parameters (species diffusivity, heat conductivity, dynamic viscosity) are computed at every grid point using the species concentrations and temperature. The transport parameters are computed using the following molecular properties: their Lennard Jones potential well depth, collision diameter, dipole moment, polarizability, and their rotational relaxation collision number. The molecular properties are obtained from

Kee *et al.*³³. Again, since the properties of some species were not available, they had to be substituted with other ones. In particular, the molecular properties of GaCl and As₄ were substituted with that of GaH and As₂.

Appendix D: Cracking model validation and center port surrogate model

The two assumptions used to derive the cracking model namely the 1D advection-reaction approximation and the sole dependence of density on temperature are addressed. The model is compared to three-dimensional reacting flow simulations. The validation of these assumptions will further bolster the correction applied to the cracking kinetic coefficients.

The 1D transport of enthalpy in a cylindrical tube neglecting axial diffusion can be approximated as

$$\frac{d}{dx}(\rho U C_p T) \pi R^2 dx = h(T_w(x) - T(x)) 2\pi R dx, \quad (D1)$$

where ρ is the local density, C_p is the local heat capacity, $T(x)$ is the local temperature, $T_w(x)$ is the wall temperature and R is the tube radius and h is the convective heat transfer coefficient. The convective heat transfer coefficient for a fully developed pipe flow can be obtained from Nusselt number $Nu = 3.66^{34}$. The heat transfer coefficient can be written as $h \approx Nu\lambda / (R)$ where λ is the thermal conductivity. Assuming a near-constant heat capacity and neglecting the addition of mass due to surface reactions

$$\frac{dT}{dx} = \frac{2h}{R\rho_0 U_0 C_p} (T_w(x) - T(x)), \quad (D2)$$

where ρ_0 , U_0 , and C_p are the fluid properties at the pipe inlet. The same approach for the transport of mass fraction of AsH₃ leads to

$$\frac{dY_{AsH_3}}{dx} = \frac{-2Y_{AsH_3} A_{cracking}}{R\rho_0 U_0} e^{\frac{-E_{a,cracking}}{R_u T_w(x)}} \frac{\rho_0 T_0}{T(x)}, \quad (D3)$$

where $\rho(x)$ was assumed to be solely a function of temperature. Given a 1D discretization, Eqs. D2 and D3 can be solved with an exponential type of integrator such as a Rosenbrock integrator.

In Fig. 12 the results for a 3D reacting flow simulation are shown for conditions similar to the ones of DenBaars *et al.*⁹. The wall temperature is held fixed at 723.15 K and 773.15 K, the cylinder radius is 25 mm, its length is 125 mm, the pressure is 1 atm, and the inlet is made of 50% AsH₃ and H₂ by volume. The mesh size is 1.5 mm radially and 4 mm axially.

The profile of Y_{AsH_3} exhibits variation within a cross-section due to the relatively larger diameter. Nevertheless, the 1D model successfully approximates the longitudinal profile of Y_{AsH_3} . In turn, it suggests that the correction for the kinetic rate for arsine cracking is valid.

The same procedure can be applied to the center port of the HVPE reactor studied in this work. In this case, the cylinder

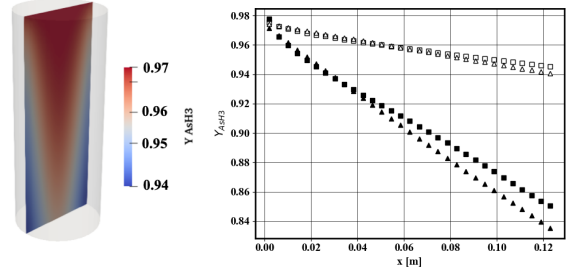


FIG. 12. Left: contour of mass fraction of AsH₃ in a cylinder that replicates the experiments⁹. Flow is from top to bottom. Right: surface averaged longitudinal profile of mass fraction of AsH₃ for a wall temperature of 723.15 K for the 3D model (□) and the 1D model (△) and for a wall temperature of 773.15 K for the 3D model (■) and the 1D model (▲).

has a 2 mm radius and its length is 308 mm. The center port is even more suited to the 1D approximation given its larger length to radius ratio. The wall temperature is held fixed at 1023.15 K, and the pressure is 0.829 atm. The mesh size is 0.12 mm radially and 4 mm axially. The results are shown in Fig. 13. Since the aspect ratio of the cylinder is smaller than that of DenBaars *et al.*⁹, the profile of AsH₃ is almost one dimensional (left). In turn, the 1D model accurately reproduces the longitudinal profile of AsH₃.

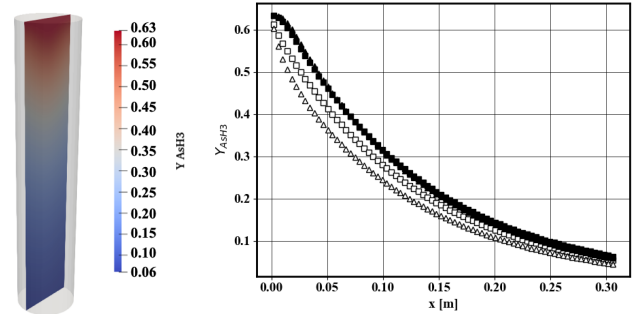


FIG. 13. Left: contour of mass fraction of AsH₃ in a cylinder that replicates the center port. The longitudinal direction was rescaled by a factor 0.032 for plotting purposes. Flow is from top to bottom. Right: surface averaged longitudinal profile of mass fraction of AsH₃ for an outer-wall temperature of 1023.15 K without taking into account the heat transfer through the quartz for the 3D model (□) and the 1D model (△), and by taking into account the heat transfer through the quartz for the 3D model (■) and the 1D model (▲).

In the experiments reported in Schulte *et al.*⁷, the center port has an inner radius $R_{in} = 2$ mm and an outer radius of $R_{out} = 4.5$ mm. One can also incorporate the conjugate heat transfer between the quartz annulus and the inner flow. The inner-wall temperature can be obtained by writing a balance of heat flux at the inner-wall boundary

$$h(T(x) - T_{iw}(x)) + \frac{\lambda_{quartz}}{\Delta R} (T_w(x) - T_{iw}(x)) = 0, \quad (D4)$$

where λ_{quartz} is the heat conductivity of the quartz, T_{iw} is the inner-wall temperature, T_w is the outer-wall temperature and $\Delta R = R_{out} - R_{in}$. An algebraic expression can be obtained for T_{iw} , and Eq. D2 becomes

$$\frac{dT}{dx} = \frac{2h}{R\rho_0 U_0 C p_0 \left(1 + \frac{h\Delta R}{\lambda_{quartz}}\right)} (T_w(x) - T(x)), \quad (D5)$$

and Eq. D3 becomes

$$\frac{dY_{AsH_3}}{dx} = \frac{-2Y_{AsH_3}}{R\rho_0 U_0} A_{cracking} e^{-E_{cracking}/(R_u T_{iw}(x))} \frac{\rho_0 T_0}{T(x)}, \quad (D6)$$

$$\text{where } T_{iw}(x) = T(x) + \frac{T_w(x) - T(x)}{1 + h\Delta R/\lambda_{quartz}}.$$

The 1D model is compared to a 3D model run with CFD, where the heat transfer through the solid is written assuming constant thermodynamic and transport properties

$$\frac{\partial}{\partial t} (\rho_{quartz} T) = \frac{1}{C p_{quartz}} \nabla \cdot (\lambda_{quartz} \nabla T), \quad (D7)$$

where ρ_{quartz} is the density of the solid assumed to be equal to $2200 \text{ kg}\cdot\text{m}^{-3}$, $C p_{quartz}$ is the heat capacity of the solid set at $705 \text{ J}\cdot\text{kg}^{-1}\cdot\text{K}^{-1}$, and λ_{quartz} is equal to $1.46 \text{ W}\cdot\text{m}^{-1}\cdot\text{K}^{-1}$. The coupling between the solid and fluid equations is performed via outer-Picard iterations²¹. The thermal coupling at every face of the inner-wall boundary is done by dynamically setting the inner-wall temperature to

$$T_{iw} = \frac{T_s \frac{\lambda_s}{\Delta s} + T_f \frac{\lambda_{fluid}}{\Delta f}}{\frac{\lambda_s}{\Delta s} + \frac{\lambda_{fluid}}{\Delta f}}, \quad (D8)$$

where T_s (respectively T_f) is the temperature in the solid (respectively fluid) domain that is radially adjacent to the inner-wall face, λ_s (respectively λ_f) is the heat transfer coefficient at that same location, Δs (respectively Δf) is the distance between that location and the inner-wall face center. The choice of the inner-wall temperature boundary condition equates both the temperature and the heat flux at the inner-wall interface. The mesh size is the same as the one used without the conjugate heat transfer, and the results are shown in Fig. 13 (right) for an outer-wall temperature of 1023.15 K . The 1D model and the 3D model reasonably agree on the longitudinal profile of AsH_3 . Because the inner-wall temperature is lower than without the conjugate heat transfer, less AsH_3 cracks through the center port. Similar to the results shown in Fig. 12, since the 1D model neglects radial diffusion, it overestimates the amount of AsH_3 immediately adjacent to the walls, thereby slightly overestimating the amount of AsH_3 cracked.

Overall, the 1D model is a reasonable representation at lower computational costs for modeling transport and chemistry within the center port and it is proposed to be used as a surrogate for the flow inside the center port to obtain the boundary conditions at the exit of the injector. The boundary

conditions for velocity can be obtained from mass conservation assuming that it solely depends on the density at the exit of the tube which, in turn, is assumed to be a sole function of temperature. The mass fraction of As_4 at the center port exit can be computed by integrating Eq. D6 over the length of the tube.

In the CFD model, the surrogate model is implemented by first collecting the value of temperature (transported according to Eq. A3) at the outer-walls of the center port, at every timestep. The temperature values are averaged azimuthally to construct a one-dimensional representation of the outer-wall temperature of the center port. The one-dimensional wall temperature profile is then directly used in the advection-reaction model of the center port. The boundary conditions at the injector exit are subsequently evaluated by integrating the 1D ordinary differential equation systems (Eqs. D5 and D6) for the scalars and temperature. This procedure allows incorporating longitudinal gradients of temperature along the center-port walls into the center-port exit boundary condition. Although the method is repeated at every timestep, the overhead computational cost is negligible compared to momentum and scalar transport.

Appendix E: Effect of prior on the Bayesian calibration

In Bayesian analysis, the posterior distribution depends on the prior, which in turn may have an effect on the PDF of the calibrated K_{react} . In the results reported in the paper, the prior was chosen to be $\mathcal{U}(10^4, 2 \times 10^7)$ for $A_{cracking}$ and $\mathcal{U}(0, 10)$ for σ . In Fig. 14, the results are reported with a narrow prior $\mathcal{U}(10^5, 10^6)$ for $A_{cracking}$ and $\mathcal{U}(0, 1)$ for σ ; and a wide prior $\mathcal{U}(1, 2 \times 10^{11})$ for $A_{cracking}$ and $\mathcal{U}(0, 100)$ for σ . As can be observed, the prior has little effect on the posterior distribution of $A_{cracking}$.

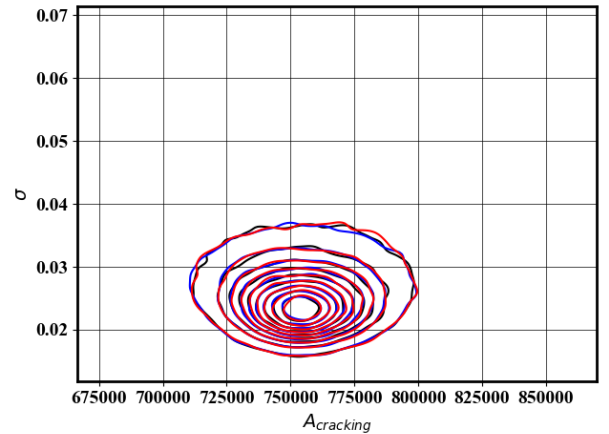


FIG. 14. Black line: Two-dimensional posterior PDF for prior used ($\mathcal{U}(10^4, 2 \times 10^7)$ for $A_{cracking}$ and $\mathcal{U}(0, 10)$ for σ). Blue line: Two-dimensional posterior PDF for narrow prior ($\mathcal{U}(10^5, 10^6)$ for $A_{cracking}$ and $\mathcal{U}(0, 1)$ for σ). Red line: Two-dimensional posterior PDF for wide prior ($\mathcal{U}(1, 2 \times 10^{11})$ for $A_{cracking}$ and $\mathcal{U}(0, 100)$ for σ).

Appendix F: Infinitely fast kinetic growth model

An infinitely fast kinetic model is implemented following the hypothesis that the reactor operates in a transport-limited regime. A mass flux boundary condition is imposed for the species transport equations at the substrate using the reactant composition at adjacent computational cells. Molar stoichiometry is used to determine excess and deficient reactants at the surface and surface gradients are subsequently set to match the desired consumption rate.

The growth rate results are reported for Case 2 and Case 3 in Tab. II. While the order of magnitude of the growth rates obtained with the infinitely fast chemistry is reasonable and has the correct trend compared to experiments, it leads to growth rates about 2 times larger (third row) than the ones observed in the experiments (second row). We conclude that a simple transport-limited description of the reaction cannot accurately explain the growth rate of GaAs via uncracked hydrides.

TABLE II. Growth rates of Case 2 and 3 obtained with infinitely fast chemistry.

	R_G [$\mu\text{m}/\text{h}$] for Case 2	R_G [$\mu\text{m}/\text{h}$] for Case 3
Schulte <i>et al.</i> ⁷	28.8	63.2
Infinitely fast	59.1	125.1

- ¹R. R. King, C. M. Fetzer, D. C. Law, K. M. Edmondson, H. Yoon, G. S. Kinsey, D. D. Krut, J. H. Ermer, P. Hebert, B. T. Cavicchi, *et al.*, "Advanced III-V multijunction cells for space," in *2006 IEEE 4th World Conference on Photovoltaic Energy Conference*, Vol. 2 (IEEE, 2006) pp. 1757–1762.
- ²R. Hoheisel, S. Philipps, and A. Bett, "Long-term energy production of III-V triple-junction solar cells on the Martian surface," *Progress in Photovoltaics: Research and Applications* **18**, 90–99 (2010).
- ³J. Simon, K. L. Schulte, K. A. Horowitz, T. Remo, D. L. Young, and A. J. Ptak, "III-V-based optoelectronics with low-cost dynamic hydride vapor phase epitaxy," *Crystals* **9**, 3 (2019).
- ⁴E. L. McClure, K. L. Schulte, J. Simon, W. Metaferia, and A. J. Ptak, "GaAs growth rates of 528 $\mu\text{m}/\text{h}$ using dynamic-hydride vapor phase epitaxy with a nitrogen carrier gas," *Applied Physics Letters* **116**, 182102 (2020).
- ⁵W. Metaferia, K. L. Schulte, J. Simon, S. Johnston, and A. J. Ptak, "Gallium arsenide solar cells grown at rates exceeding 300 $\mu\text{m}/\text{h}$ by hydride vapor phase epitaxy," *Nature communications* **10**, 1–8 (2019).
- ⁶K. A. Horowitz, T. W. Remo, B. Smith, and A. J. Ptak, "A techno-economic analysis and cost reduction roadmap for III-V solar cells," Tech. Rep. (National Renewable Energy Lab.(NREL), Golden, CO (United States), 2018).
- ⁷K. L. Schulte, A. Braun, J. Simon, and A. J. Ptak, "High growth rate hydride vapor phase epitaxy at low temperature through use of uncracked hydrides," *Applied Physics Letters* **112**, 042101 (2018).
- ⁸L. Hollan and J. Durand, "Fast growth in GaAs VPE at low temperature and high partial pressures," *Journal of Crystal Growth* **46**, 665–670 (1979).
- ⁹S. DenBaars, B. Maa, P. Dapkus, A. Danner, and H. C. Lee, "Homogeneous and heterogeneous thermal decomposition rates of trimethylgallium and arsine and their relevance to the growth of GaAs by MOVPE," *Journal of Crystal Growth* **77**, 188–193 (1986).
- ¹⁰D. W. Shaw, "Kinetic aspects in the vapour phase epitaxy of III-V compounds," *Journal of crystal growth* **31**, 130–141 (1975).
- ¹¹Y. Kangawa, T. Ito, Y. Hiraoka, A. Taguchi, K. Shiraishi, and T. Ohachi, "Theoretical approach to influence of As₂ pressure on GaAs growth kinetics," *Surface science* **507**, 285–289 (2002).
- ¹²D. L. Young, A. J. Ptak, T. F. Kuech, K. Schulte, and J. D. Simon, "High throughput semiconductor deposition system," (2013), uS Patent App. 13/895,190.

- ¹³R. M. Biefeld, D. D. Koleske, and J. G. Cederberg, "The Science and Practice of Metal-Organic Vapor Phase Epitaxy (MOVPE)," in *Handbook of Crystal Growth* (Elsevier, 2015) pp. 95–160.
- ¹⁴K. L. Schulte, W. Metaferia, J. Simon, and A. J. Ptak, "Uniformity of GaAs solar cells grown in a kinetically-limited regime by dynamic hydride vapor phase epitaxy," *Solar Energy Materials and Solar Cells* **197**, 84–92 (2019).
- ¹⁵K. L. Schulte, J. Simon, N. Jain, D. L. Young, and A. J. Ptak, "A kinetic model for GaAs growth by hydride vapor phase epitaxy," in *2016 IEEE 43rd Photovoltaic Specialists Conference (PVSC)* (IEEE, 2016) pp. 1930–1933.
- ¹⁶M. Harrous, L. Chaput, A. Bendraoui, M. Cadoret, C. Pariset, and R. Cadoret, "Phosphine and arsine decomposition in CVD reactors for InP and InGaAs growth," *Journal of Crystal Growth* **92**, 423–431 (1988).
- ¹⁷K. Braman, T. A. Oliver, and V. Raman, "Bayesian analysis of syngas chemistry models," *Combustion Theory and Modelling* **17**, 858–887 (2013).
- ¹⁸J. Bell, M. Day, J. Goodman, R. Grout, and M. Morzfeld, "A bayesian approach to calibrating hydrogen flame kinetics using many experiments and parameters," *Combustion and Flame* **205**, 305–315 (2019).
- ¹⁹K. Grüter, M. Deschler, H. Jürgensen, R. Beccard, and P. Balk, "Deposition of high quality GaAs films at fast rates in the LP-CVD system," *Journal of crystal growth* **94**, 607–612 (1989).
- ²⁰F. Pedregosa, G. Varoquaux, A. Gramfort, V. Michel, B. Thirion, O. Grisel, M. Blondel, P. Prettenhofer, R. Weiss, V. Dubourg, J. Vanderplas, A. Passos, D. Cournapeau, M. Brucher, M. Perrot, and E. Duchesnay, "Scikit-learn: Machine Learning in Python," *Journal of Machine Learning Research* **12**, 2825–2830 (2011).
- ²¹M. Hassanaly, H. Koo, C. F. Lietz, S. T. Chong, and V. Raman, "A minimally-dissipative low-Mach number solver for complex reacting flows in OpenFOAM," *Computers & Fluids* **162**, 11–25 (2018).
- ²²M. Hassanaly, Y. Tang, S. Barwey, and V. Raman, "Data-driven Analysis of Relight variability of Jet Fuels induced by Turbulence," *Combustion and Flame* **225**, 453–467 (2020).
- ²³Y. Tang and V. Raman, "Large eddy simulation of premixed turbulent combustion using a non-adiabatic, strain-sensitive flamelet approach," *Combustion and Flame* **234**, 111655 (2021).
- ²⁴H. Koo, M. Hassanaly, V. Raman, M. E. Mueller, and K. Peter Geigle, "Large-eddy simulation of soot formation in a model gas turbine combustor," *Journal of Engineering for Gas Turbines and Power* **139** (2017).
- ²⁵H. Sitarman, S. Yellapantula, M. T. H. de Frahan, B. Perry, J. Rood, R. Grout, and M. Day, "Adaptive mesh based combustion simulations of direct fuel injection effects in a supersonic cavity flame-holder," *Combustion and Flame* **232**, 111531 (2021).
- ²⁶J. Smagorinsky, "General circulation experiments with the primitive equations: I. The basic experiment," *Monthly weather review* **91**, 99–164 (1963).
- ²⁷Y. Tang, M. Hassanaly, V. Raman, B. Sforzo, and J. Seitzman, "A comprehensive modeling procedure for estimating statistical properties of forced ignition," *Combustion and Flame* **206**, 158–176 (2019).
- ²⁸M. Maestri and A. Cuoci, "Coupling CFD with detailed microkinetic modeling in heterogeneous catalysis," *Chemical Engineering Science* **96**, 106–117 (2013).
- ²⁹G. Strang, "On the construction and comparison of difference schemes," *SIAM journal on numerical analysis* **5**, 506–517 (1968).
- ³⁰C. Heye, V. Raman, and A. R. Masri, "LES/probability density function approach for the simulation of an ethanol spray flame," *Proceedings of the Combustion Institute* **34**, 1633–1641 (2013).
- ³¹S. T. Chong, M. Hassanaly, H. Koo, M. E. Mueller, V. Raman, and K.-P. Geigle, "Large eddy simulation of pressure and dilution-jet effects on soot formation in a model aircraft swirl combustor," *Combustion and Flame* **192**, 452–472 (2018).
- ³²M. A. Oehlschlaeger, J. Steinberg, C. K. Westbrook, and W. J. Pitz, "The autoignition of iso-cetane at high to moderate temperatures and elevated pressures: Shock tube experiments and kinetic modeling," *Combustion and flame* **156**, 2165–2172 (2009).
- ³³R. Kee, G. Dixon-Lewis, J. Warnatz, M. Coltrin, J. Miller, and H. Moffat, "Transport: a software package for the evaluation of gas-phase, multicomponent transport properties," *Chemkin Collection* (1999).
- ³⁴T. L. Bergman, F. P. Incropera, D. P. DeWitt, and A. S. Lavine, *Fundamentals of heat and mass transfer* (John Wiley & Sons, 2011).